THE JOURNAL OF PHYSICAL CHEMISTRY A
A JOURNAL OF THE AMERICAN CHEMICAL SOCIETY

pubs.acs.org/JPCA

Article

Generative Adversarial Neural Networks for Denoising Coherent Multidimensional Spectra

Ziareena A. Al-Mualem and Carlos R. Baiz*

Cite This: https://doi.org/10.1021/acs.jpca.2c02605

Read Online

ACCESS | Metrics & More | Article Recommendations | Supporting Information

ABSTRACT: Ultrafast spectroscopy often involves measuring weak signals and long data acquisition times. Spectra are typically collected as a "pump−probe" spectrum by measuring differences in intensity across laser shots. Shot-to-shot intensity fluctuations are most often the primary source of noise in ultrafast spectroscopy. Here, we present a novel approach for denoising ultrafast two-dimensional infrared (2D IR) spectra using conditional generative adversarial neural networks (cGANNs). The cGANN approach is able to eliminate shot-to-shot noise and reconstruct the line shapes present in the noisy input spectrum. We present a general approach for training the cGANN using matched pairs of noisy and clean synthetic 2D IR spectra based on the Kubo-line shape model for a three-level system. Experimental shot-to-shot laser noise is added to synthetic spectra to recreate the noise profile present in measured experimental spectra. The cGANNs can recover line shapes from synthetic 2D IR spectra with signal-to-noise ratios as low as 2:1, while largely preserving the key features such as center frequencies, line widths, and diagonal elongation. In addition, we benchmark the performance of the cGANN using experimental 2D IR spectra of an ester carbonyl vibrational probe and demonstrate that, by applying the cGANN denoising approach, we can extract the frequency−frequency time correlation function (FFCF) from reconstructed spectra using a nodal-line slope analysis. Finally, we provide a set of practical guidelines for extending the denoising method to other coherent multidimensional spectroscopies.

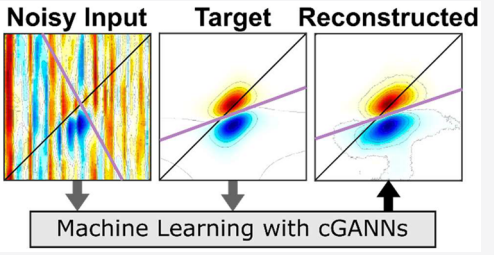

INTRODUCTION

Coherent multidimensional spectroscopy (CMDS) techniques measure time-resolved molecular structures and dynamics in heterogeneous systems. Measurements are typically done by applying a sequence of laser pulses to measure the nonlinear vibrational or electronic polarization of a system.[1−3] Nonlinear signals are approximately 3 orders of magnitude lower in amplitude compared to the applied laser pulses. The weak nonlinear signals are heterodyned with a strong local oscillator to reconstruct the signal electric field amplitude and phase.[2,4] Shot-to-shot subtraction is essential to isolate specific signals of interest. Since the local oscillator pulse amplitudes are usually greater than the nonlinear signals, subtraction is highly susceptible to laser intensity fluctuations. As a consequence, signal-to-noise ratios (SNRs) in ultrafast measurements are dominated by instabilities in the laser output intensity as well fluctuations within the optical setup, such as air currents, thermal gradients, and optomechanical drift.[5−7] This makes certain measurements particularly challenging, and in some cases, the measurement of single multidimensional spectra requires acquisition times of several hours to several days.[8−11]

Low SNRs and long data acquisition times are arguably the most severe limitations of ultrafast spectroscopy. Significant efforts have resulted in several effective noise suppression schemes. These approaches can be roughly divided into two categories: (1) methods implemented within the design of the optical setup[9,12−16] and (2) numerical models for on-the-fly processing of measured laser shots and postprocessing methods.[17−22] The first category includes passive methods such as using common optical components or active methods that monitor and correct for optical drift.[23−26] These methods typically target intensity fluctuations and phase drift as well as spectral shifts, which are the main sources of noise in ultrafast spectroscopy. High-repetition rate lasers and fast interferometric scanning can further mitigate the $1/f$ laser noise.[27−32] In addition, it is common to use a secondary detector, where a copy of the probe spectrum can be detected simultaneously with and without the nonlinear signal of interest.[6,7,33,34] Within this category, on-the-fly data processing can be used to suppress fluctuations by either directly referencing "blank" pixels or taking advantage of spatial correlations between pulses measured across two detectors.[17−19,35] Combinations of these noise suppression methods have significantly improved the quality of data produced in ultrafast measurements. Despite these advancements, collecting high-quality data sets remains a bottleneck for ultrafast spectroscopy. For these reasons, there

Received: April 15, 2022
Revised: May 19, 2022

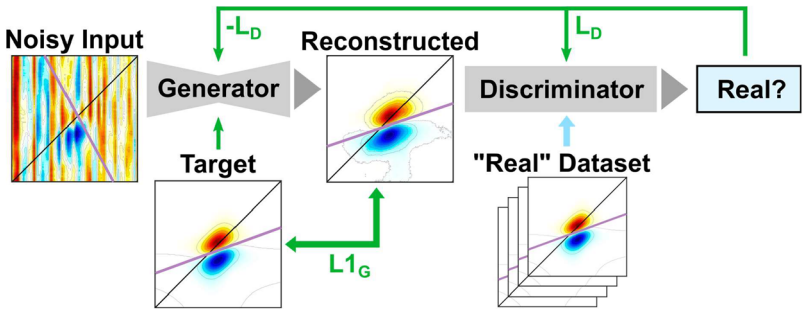

Figure 1. Diagram of the conditional generative adversarial neural network (cGANN) architecture and general training approach. The generator is simultaneously trained on a combination of two L1 loss functions: one derived from the output of the discriminator (L_D) and one on the difference between generated and target spectra ($L1_G$).

is a pressing need to develop robust denoising methods that can be either implemented for on-the-fly processing or used to denoise data post acquisition. Here, we present a method to reconstruct spectral line shapes from noisy spectra.

Machine learning (ML) is perhaps one of the most useful computational tools that has emerged in the past decade. ML provides a general approach to extract features from large data sets without preset physical models.[36−41] Indeed, ML implementations are now commonplace, not only in science, but ML has transformed nearly all modern consumer electronics. For example, ML models are now an integral part of the image-processing workflow in cell phone photography, particularly because ML models are well suited for image analysis and processing.[41,42] In particular, conditional generative adversarial neural networks (cGANNs) have been developed as a general tool for image-to-image translation from an input domain to an output domain.[43−45] cGANNs are perfectly suited to image processing applications such as removing artifacts, reducing noise, or generating missing features. In short, the cGANN architecture is composed of a generator convolutional neural network, which generates sets of images, and a corresponding discriminator, which distinguishes between images derived from the training set versus the generated image set (Figure 1).[44,46,47] Here, the cGANN model "learns" the general features present in the training data and can reconstruct spectra that contain the same features present in the training set.[45,48] This makes the model perfectly suited to extract these features from noisy images and generate the corresponding "denoised" or reconstructed images, specifically, for denoising experimental ultrafast spectra where the underlying features, such as the general number of peaks and frequencies, are often known *a priori*, but the new information is contained in the subtle changes to the line shapes with varying experimental conditions. Therefore, it is straightforward to generate synthetic training spectra that contain the general features of the measured spectra and use synthetic image pairs to train the cGANN. In this paper, we demonstrate the use of cGANNs for denoising two-dimensional infrared (2D IR) spectra and describe a general procedure for the generation of synthetic spectra based on the Kubo line shape model but with added experimental laser noise.

METHODS

Experimental Two-Dimensional Infrared Spectroscopy. The 2D IR spectrometer has been described previously.[49] In brief, mid-IR pulses (100 fs, ∼300 cm^{-1}) are generated using a combination of optical parametric amplification and difference-frequency generation (TOPAS Prime/N-DFG, Light Conversion), which is pumped by a 1 kHz Ti:sapphire-based regenerative amplifier (Astrella, Coherent Inc.) The 25 μJ mid-IR pulses are split into excitation (pump) pulses and detection (probe) pulses using a 0.5 °CaF_2 wedge. The excitation pulses are routed through an acoustooptical-based pulse shaper (QuickShape, PhaseTech Spectroscopy)[50] to generate time-delayed pulse pairs. Each delay is repeated twice in which the carrier phase of the stationary pulse is modulated by π, thus producing adjacent "0 0" and "0 π" pulses, which are subtracted to recover the 2D IR signal and suppress pump−probe scatter. The delay between the pump pulses is numerically Fourier-transformed to generate the excitation frequency axis. The probe pulse is measured using a 128 × 128-pixel MCT array detector (Catalina, Teledyne Nova Sensors),[51] which is used to generate the detection frequency axis. The pump and probe pulses were maintained at perpendicular polarizations to reduce pump scatter at the detector.

We measured 2D IR spectra of the single-peak carbonyl stretch of dilute ethyl acetate (EtOAc) (99.8%; Sigma-Aldrich) in dimethyl sulfoxide (DMSO) (>99.7%; Fisher BioReagents) at a concentration of 0.25 mg/mL at room temperature and under dry air. All chemicals were used as received. The spectra were collected at coherence times (t_1) scanned from 0 to 3 ps in steps of 20 fs to generate the excitation axis (ω_1) by numerical Fourier transformation. The waiting times (t_2) were selected at intervals ranging from 150 fs to 3 ps. Spectra were collected with a rotating frame frequency of 1400 cm^{-1}. The individual noisy spectra at each waiting time were collected by averaging 4000 laser shots (∼4 s of data acquisition), and the final clean spectra were an average of 800 000 laser shots (∼13 min of data acquisition). The 2D IR spectra were normalized to the highest intensity peak in the frequency domain. The data set was collected over a period of ∼8 h of continuous laser operation. Blank shots were collected at a different time by setting the waiting time to −10 ps, such that the probe arrives at the sample before the pump, resulting in spectra without the third-order signal. In total, 100 sets of 128 pixels by 10 000 blank shots were measured sequentially, stored, and later used to generate synthetic spectra with experimental noise, as described next.

Response Functions and Experimental Laser Noise. Time-domain response functions were generated using the standard three-level Kubo line shape model as described previously and are numerically Fourier-transformed to generate 2D IR spectra.[3,52] Specifically, within the Kubo model, the frequency−frequency correlation function is assumed to reflect

https://doi.org/10.1021/acs.jpca.2c02605
J. Phys. Chem. A XXXX, XXX, XXX−XXX

Table 1. Response Function Parameters Used for cGANN Training

	parameter						
	ω_{01} (cm^{-1})	Δ (cm^{-1})	$\Delta\omega$ (cm^{-1})	τ_c (ps)	T_2^* (ps)	χ (arb)	μ_{01} (arb)
min	1680	12.8	5	1.5	1	1	1
max	1712	19.2	20	1.5	4	1	1

sub-100 fs relaxation, resulting from inertial dynamics, followed by single-exponential picosecond relaxation:

$$C(t) = \Delta\omega^2 e^{-t/\tau_c} + \frac{\delta(t)}{T_2^*} \tag{1}$$

The following line shape function is produced:

$$g(t) = \Delta\omega^2 \tau_c^2 \left(e^{-t/\tau_c} + \frac{t}{\tau_c} - 1 \right) + \frac{t}{T_2^*} \tag{2}$$

where $\Delta\omega$ is the amplitude of frequency fluctuations, τ_c is the frequency−fluctuation correlation decay time, $\delta(t)$ represents the limit of fast dynamics, and T_2^* is the pure dephasing time. The fast relaxation is below the time resolution of the 2D IR spectrometer. The line shape function is then used to generate spectra using the associated response functions for the rephasing (R_r) and nonrephasing (R_{nr}) signals respectively:

$$R_r = 2\chi i {\mu_{01}}^4 (e^{-i(\omega_{01}-\omega_{rot})(t_3-t_1)} - e^{-i[(\omega_{01}-\omega_{rot}-\Delta)t_3-(\omega_{01}-\omega_{rot})t_1]}) \times e^{-g(t_1)+g(t_2)-g(t_3)-g(t_1+t_2)-g(t_2+t_3)+g(t_1+t_2+t_3)} \times e^{-t_2/T_1} \tag{3}$$

$$R_{nr} = 2\chi i {\mu_{01}}^4 (e^{-i(\omega_{01}-\omega_{rot})(t_3+t_1)} - e^{-i[(\omega_{01}-\omega_{rot}-\Delta)t_3+(\omega_{01}-\omega_{rot})t_1]}) \times e^{-g(t_1)-g(t_2)-g(t_3)+g(t_1+t_2)+g(t_2+t_3)-g(t_1+t_2+t_3)} \times e^{-t_2/T_1} \tag{4}$$

in which χ is a scaling factor to account for the number of oscillators, μ_{01} is the transition dipole moment of the oscillator, ω_{01} is the center frequency of the transition, ω_{rot} is a rotating-frame frequency, Δ is the anharmonicity, t_1, t_2, and t_3 are the three corresponding time delays, respectively, and T_1 is the vibrational lifetime of the transition. The total response function is the sum of the rephasing and nonrephasing signals. This function is then Fourier-transformed along t_1 and t_3 to generate a complex signal $S_{2DIR}(\omega_1, t_2, \omega_3)$ that is comparable to the 2D IR measurements. The t_1 axis is chosen to be the same as the t_1 steps measured in the experiment.

In typical experimental 2D IR spectra, the intensities of the ground state-bleach and excited state-absorption peaks do not match as a result of anharmonicities, non-Condon effects, and other solvation effects[53] that affect the line shapes for the $\nu_{1\to2}$ transition. In principle, this can also be incorporated in the training set by modifying the values of the transition dipole moments for the $\nu_{0\to1}$ and $\nu_{1\to2}$ transitions in the Kubo model.[54,55] The cGANN model is agnostic with respect to the training set, so more complex line shapes, such as those derived from molecular dynamics simulations or vibrational maps, can be used for training. The non-Condon coefficient may be included in the line shape mode for systems where the Condon approximation fails.

Next, a series of "blank" experimental probe shots are used to generate the noise contributions to the spectra. Sets were selected at random to generate a sequence of 15 000 shots. This sequence was then split into pulse pairs, chosen to represent the "0 0" and "0 π" shots in the experimental measurements, and the pulses are pairwise subtracted. This noise trajectory is then split into sequential sets containing the same number of elements as the t_1 delays in the 2D IR measurement (151 delays), and the sets are then averaged together. The subsequent laser shot noise series is Fourier-transformed to obtain ω_1 and ω_3 noise spectra. Next, the noise spectra are interpolated to the same ω_1 and ω_3 axes as the S_{2DIR} signal. Finally, the noise spectrum is normalized by the root-mean-squared (RMS) amplitudes across all frequencies and then multiplied by a scaling factor to produce the desired signal-to-noise ratio (SNR) of the synthetic spectrum. Here, the signal-to-noise ratio is defined as the ratio of the maximum amplitude of the 2D IR signal prior to noise addition (S_{2DIR}) to the RMS amplitude of the noise floor. The 2D IR signal and the noise spectrum are then added together to generate the final noisy spectrum. Each set is exported as a pair of two single-channel 8-bit uncompressed images corresponding to the spectra with and without noise, which then serve as the labeled pairs for cGANN training.

Synthetic Spectra Generated for Training. Synthetic spectra were generated using the three-level response function and experimental noise profiles described above. The training set consisted of 1000 total synthetic spectra as five sets of 200 spectra, with four sets with increasing signal-to-noise ratios from 2 to 5, 10, and 20, and one set without noise. Using the same parameters, an additional set of 200 spectra within each SNR was generated for benchmarking. The waiting time (t_2) was randomly selected from 150 fs to 3 ps. The response function parameters were randomly selected from a uniform distribution within the parameter bounds shown in Table 1, and the random experimental noise was added to each spectrum individually. The noise trajectories and source code used to generate the synthetic spectra are available on GitHub (https://github.com/baizgroup/SyntheticSpectra).

The frequency−fluctuation correlation decay time in the training set can be within a relatively broad range of values to avoid biasing the cGANN. However, it is important to mention that the denoising does not include any t_2 information, so the only important consideration is that the training set must have peaks with diagonal elongation that are representative of the experimental spectra to be denoised.

cGANN Architecture and Training Protocol. As described above, the cGANN architecture consists of two separate neural networks: a generator and a discriminator. The cGANN loss function represents the L1 distance to the target ground truth, and the discriminator loss is used to describe whether a generated spectrum is a member of the ground truth data set. In other words, the discriminator loss is a measure of how "realistic" a spectrum is. The two loss functions are minimized simultaneously. Here, the discriminator consisted of a convolutional neural network of a depth of 8 "convolution-batch normalization-ReLU" layers with additional dropout layers for the first 4 steps, and the discriminator depth was set to 4 convolutions with a similar architecture that follows the

https://doi.org/10.1021/acs.jpca.2c02605
J. Phys. Chem. A XXXX, XXX, XXX−XXX

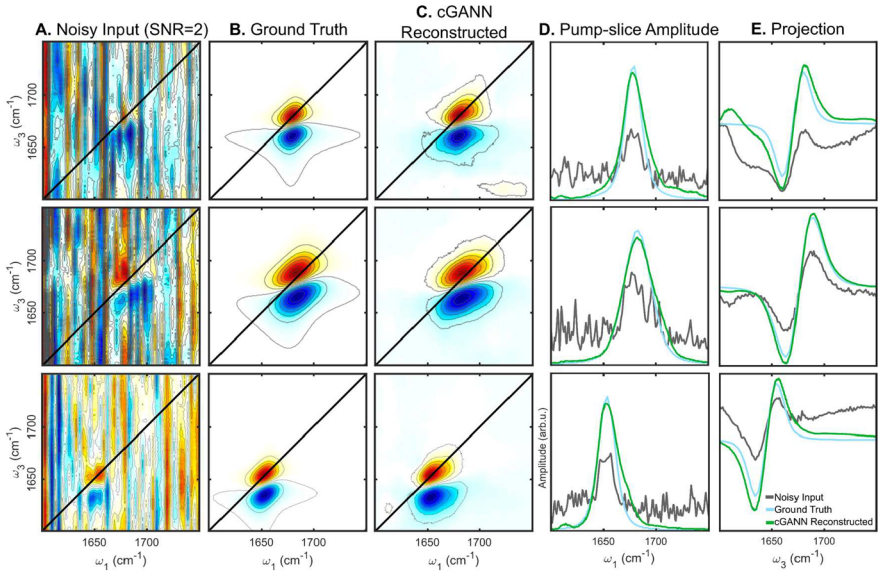

Figure 2. Example spectra as a test of the cGANN performance. (A) Synthetic spectra generated with a signal-to-noise ratio of 2 (SNR = 2) used as the input to the cGANN. (B) Ground truth "clean" spectra generated without noise. (C) cGANN reconstructed spectrum generated from the input spectrum. (D) Pump-slice amplitude and (E) probe-axis projections of the noisy input (gray), ground truth (cyan), and reconstructed (green) spectra for comparison.

implementation of Radford et al., as adopted into the pix2pix framework.[56] Here, the set of generated synthetic images was used to train the cGANN by splitting the images into 1000 mini-batches, and the training was run as a direct simultaneous steepest-decent minimization of the generator and discriminator loss for a total of 10 epochs with a learning rate for both the generator and discriminator set to 0.002, although the generator loss function quickly converged as the features present in the training spectra are relatively simple. The training data set and training scripts used here are available on GitHub (https://github.com/baizgroup/cGANN_denoising).

RESULTS AND DISCUSSION

Benchmarking Peak Center and Width. Once trained, the cGANN was benchmarked against the synthetic spectra generated using the same parameters but not included in the training set. Figure 2A shows three example noisy input spectra with an SNR of 2. These spectra contain the highest noise levels in the benchmarking set and, therefore, are the most challenging to reconstruct. The three spectra were chosen at random from the 200-spectrum benchmarking set. In all three spectra, the peaks are only just visible above the noise floor. Figure 2B shows the ground truth synthetic spectra used to generate the noisy input spectra. The first spectrum contains peaks that are relatively well centered along the pump axis; the second spectrum contains peaks around the same frequency but with broader inhomogeneous width, and the third spectrum shows a narrow peak toward the low-frequency region. In the spectra, the shot-to-shot laser noise is visible as vertical bands, as it is typically observed in experimentally measured spectra. Figure 2C shows the corresponding output spectra generated by seeding the cGANN with the corresponding noisy spectra. The reconstructed spectra have peak center frequencies and widths that are very similar to the ground truth spectra, showing that the cGANN is able to "extract" the important features from noisy spectra and generate reconstructed spectra that closely match features of the spectra in the absence of noise. Figure 2D,E shows a pump-slice amplitude (PSA) and probe-axis projection[57] of the same three spectra, respectively. The PSA analysis is described elsewhere, but in brief, the difference between the maximum and minimum amplitudes along ω_3 for a given ω_1 slice is measured. This analysis generates a spectrum that is comparable to the absorption spectrum of the same system.[58] The comparison between the reconstructed and ground truth PSA spectra in the figure more clearly shows that the reconstructed spectra closely match the ground truth. However, it is apparent that the peaks in the reconstructed spectra are slightly broader compared to the ground truth. The probe-axis projection shows that the cGANN greatly reduced the baseline shift present in the noisy spectra.

The cGANN output spectra can be more quantitively benchmarked by plotting the center frequencies and full-width-at-half-maximum (fwhm) corresponding to the benchmarking spectra. Figure 3 shows a plot of the reconstructed spectra against the ground truth for all 200 SNR = 2 spectra in the benchmarking data set. The plots show that the cGANN produces an accurate center frequency with an RMSD to ground truth of 3.1 cm^{-1} (Figure 3A). However, the spectrum appears broader, as the fwhm increases significantly with an RMSD of 6.6 cm^{-1} compared to ground truth. With the (SNR = 5) benchmarking set, the peak center and fwhm RMSD decrease to 1.9 and 4.4 cm^{-1}, respectively (Figure 3B). The results show that the cGANN denoising produces broader peaks, and this broadening is similarly observed when using higher SNR spectra as the input. This could be a result of the training set biasing the output; however, it is unclear what the origin of this broadening could be since the benchmarking set is obtained from the same parameter set as the training set. Nonetheless, the comparison shows that the cGANN can generate high-quality reconstructed spectra that closely match the features present in the noisy spectra, demonstrating that this approach is ideal for extracting features from spectra with high noise levels.

https://doi.org/10.1021/acs.jpca.2c02605
J. Phys. Chem. A XXXX, XXX, XXX−XXX

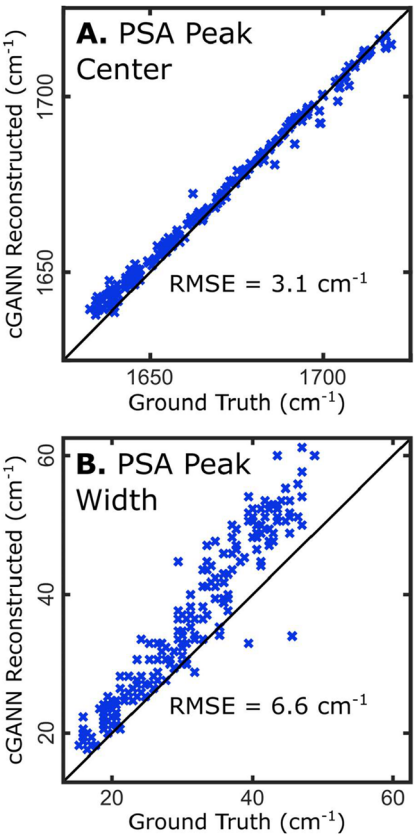

Figure 3. (A) Center peak frequencies computed as the first moment of the PSA spectrum (pump axis, ω_1) and (B) full-width-at-half-maximum of the cGANN reconstructed and ground truth spectra in the benchmarking data set using the SNR = 2 spectra as the input. The root-mean-squared-error (RMSE) for the peak center and peak width is 3.1 and 6.6 cm^{-1}, respectively.

Extracting Frequency−Frequency Correlation Functions from Reconstructed Synthetic Spectra. Two-dimensional spectroscopy is often used to extract dynamical information. Dynamics are reflected in the frequency−frequency time correlation function (FFCF) of the vibrational probe.[1,3,13,57,59−63] The correlation function can be extracted from absorptive 2D IR spectra through line shape analysis. Two commonly used methods are the center line slope (CLS) analysis and nodal-line slope (NLS) analysis.[64−71] While both methods are equivalent in the absence of noise, the NLS is more robust. In brief, NLS quantifies the slope of the nodal line between the positive ground state-bleach peak, which appears along the diagonal, and the negative excited state-absorption peak appearing below the diagonal. This is accomplished by slicing the 2D spectrum along the pump axis (ω_1) and fitting each slice to a sigmoidal function. The zero-crossing probe frequency is then used to generate the NLS. This is then fit to a line for each 2D IR spectrum, and the slope is computed. The NLS is computed for different waiting-time (t_2) spectra representing the FFCF. The decay is typically fitted to a monoexponential, and the relaxation time constant is extracted to quantify the time scale of the frequency fluctuations. One advantage of NLS over CLS is that NLS produces more robust results in the presence of pump-axis noise because a constant amplitude offset along this axis, namely, vertical stripes in 2D spectra, does not significantly affect the NLS.

Here, we quantify the ability of the cGANN to accurately reconstruct the line shapes in synthetic spectra through NLS analysis; we compare the reconstructed NLS decay with the ground truth analysis. Spectra are generated at 200 equally spaced waiting times between 150 and 3000 fs with the line shape parameters in Table 2. In brief, the parameters are within a similar range to those used in generating the training set (Table 1); however, unlike the training set, the values of the line shape parameters are fixed while generating waiting-time 2D IR spectra. One specific parameter to note is the correlation time (τ_c), which is set to 1.5 ps, and this value is then what is expected to be extracted through the NLS analysis of spectra.

Single-peak spectra generated using the response function parameters in Table 2 are shown in Figures S1, S2, and S4. It is evident that, without further processing, spectra with an SNR of 2 are inadequate for NLS line shape analysis by the randomness of the slopes shown in Figure S1. Figure 4C shows the NLS decay recovered from the waiting-time series of the noisy spectra with an SNR of 2. The random nature of the plot shows that, using traditional NLS analysis, it would be nearly impossible to extract correlation times from these highly noisy 2D IR spectra. Next, Figure 4E shows the ground truth spectra with a near-perfect single-exponential decay with a time constant of 1.5 ps. This shows that the NLS analysis recovers the correlation time used to generate the spectra as expected. It is important to note that the errors may arise from numerical noise and discrete quantization of the spectra due to the 8-bit depth used in generating the images. Finally, the same analysis is performed on the cGANN reconstructed data. The NLS shows a monoexponential decay with a time constant of 1.54 ± 0.24 ps. The error bounds are computed by the bootstrapping methods described previously.[72] In short, sets containing 50% of the data points are selected at random from the full 200-point set, and a total of 100 monoexponential fits are performed for each data set. The reported decay time constants above correspond to the average of the 100 fits, and the standard deviation across the fits is reported as the uncertainty. In conclusion, this analysis clearly shows that cGANNs can recover the NLS decay from a waiting-time 2D IR series that would be nearly impossible to analyze otherwise. The recovered NLS time constant accurately captures the dynamics of the ground truth spectra.

Extracting Frequency−Frequency Correlation Functions from Reconstructed Experimental Spectra. The performance of the cGANNs can be directly evaluated on experimental 2D IR spectra. We perform the same PSA analysis and probe-axis projection to compare the cGANN-reconstructed spectra to the noisy and clean experimental spectra (Figure 5). Here the "clean" spectra are collected at the same time as the noisy spectra but averaged over a 200×

Table 2. Response Function Parameters Used for Benchmarking cGANN Performance in Extracting Waiting-Time Dynamics

ω_{01} (cm^{-1})	Δ (cm^{-1})	$\Delta\omega$ (cm^{-1})	τ_c (ps)	T_2* (ps)	χ (arb)	μ_{01} (arb)
1675	16	20	1.5	1	1	1

https://doi.org/10.1021/acs.jpca.2c02605
J. Phys. Chem. A XXXX, XXX, XXX−XXX

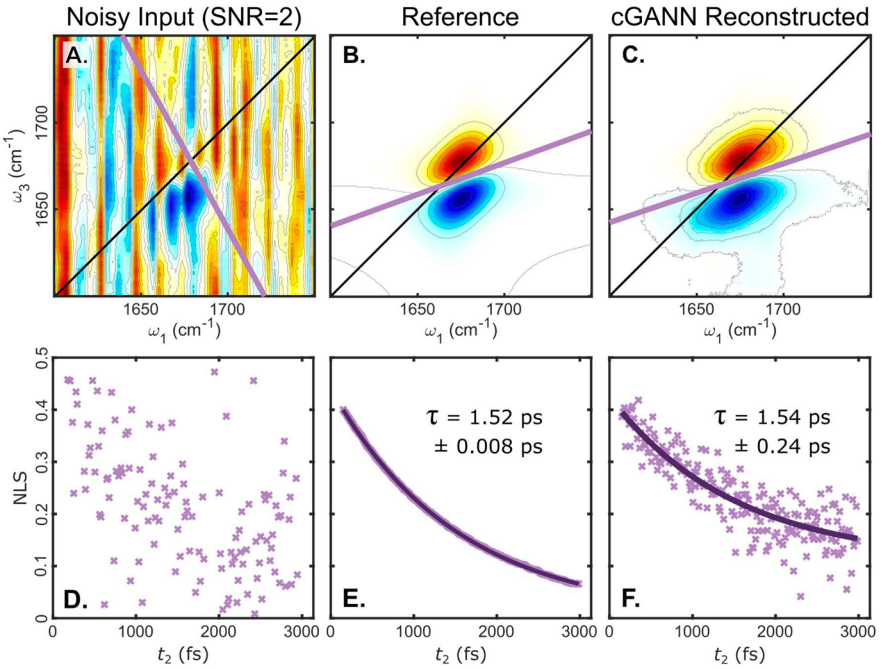

Figure 4. NLS analysis single-peak synthetic spectra. (A) Example of a noisy 2D IR spectrum (SNR = 2) at 150 fs. The purple line represents the computed NLS, shown primarily to demonstrate that NLS values cannot be extracted with such high noise levels. (B) Ground truth spectrum at the same waiting time. The spectra were generated using the response function parameters in Table 2. (C) cGANN reconstructed spectrum using the noisy spectrum as the input. (D) Recovered NLS values as a function of waiting time extracted from the analysis of noisy spectra at a signal-to-noise level of 2. Only values in the range of 0 to 0.5 are shown in this plot. The NLS values do not follow any trends, and a time scale cannot be extracted from the plot. (E) Recovered NLS decay from ground truth spectra in the absence of noise. The relaxation follows a single-exponential function with a time constant of 1.5 ps, which matches the correlation time input into the response function. (F) NLS analysis after cGANN denoising of the SNR = 2 spectra in (D). Here, the exponential relaxation is recovered and matches the time scale of the synthetic spectra without noise. The nodal line slopes of 20 selected spectra within this data set are shown in Figures S1–S3.

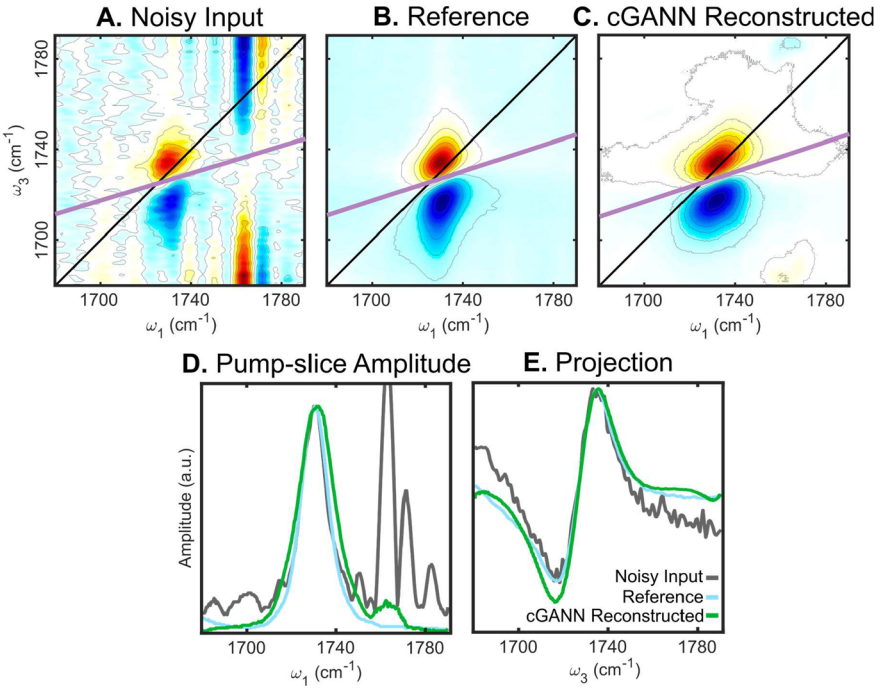

Figure 5. Example experimental 2D IR spectra of the carbonyl stretching mode of dilute ethyl acetate in DMSO. (A) Noisy spectrum with an average of 4000 laser shots collected at a waiting time of 300 fs. (B) The same spectrum but collected with much higher SNR by averaging over 800 000 shots; this is considered the ground truth spectrum. (C) Reconstructed spectrum using the noisy spectrum as the input. The purple line in (A–C) is the computed nodal line. (D) Pump-slice amplitude and (E) probe-axis projection comparisons of the noisy (gray), ground truth (cyan), and reconstructed (green) spectra. A set of 24 2D IR spectra collected at a range of waiting times are included in Figures S6–S8.

https://doi.org/10.1021/acs.jpca.2c02605
J. Phys. Chem. A XXXX, XXX, XXX–XXX

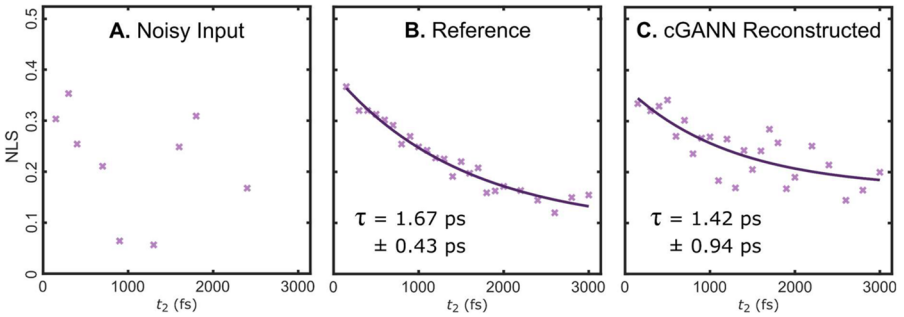

Figure 6. NLS analysis of experimental spectra of the carbonyl stretching mode of dilute ethyl acetate in DMSO. (A) NLS of the noisy spectra collected with an average of 4000 laser shots. Points that fell outside the NLS range were not included in the plot.(B) NLS of the clean spectra collected with an average of 800 000 laser shots. (C) NLS of the cGANN reconstructed spectra using the noisy data as the input. NLS analyses of a set of 24 2D IR spectra collected at a range of waiting times are included in Figures S6−S8.

greater number of shots, which produces spectra with very little noise. The spectra are processed using the same cGANN network trained from the synthetic spectra described above. Note that, since the frequency axis is not included in the cGANN training, a cGANN trained using a synthetic peak can be used for experimental (or synthetic) spectra within a different frequency range as long as the peak widths correspond to a similar fraction of the frequency axes. Similar to the analysis of synthetic spectra shown above, the reconstructed experimental spectra also closely match the "clean" reference spectra. An example set of noisy, reference, and reconstructed spectra at 300 fs are shown in Figure 5A−C, respectively. The spectra across all 24 delays are shown in Figures S6−S8. The reconstructed spectra show a slightly broader peak, as can be observed in the comparison of PSA and probe-axis projections in Figure 5D,E. Similar to the analysis described above, NLS was used to extract the dynamics from the experimental spectra. The pump-axis frequency cutoff range for computing the NLS was 1724−1745 cm^{-1}. Reliable fits could not be extracted from the noisy spectra, as shown in Figure 6A. The clean spectra and the cGANN-reconstructed spectra in Figure 6B,C show a monoexponential NLS with a decay constant of 1.67 ± 0.43 and 1.42 ± 0.94 ps, respectively. This analysis demonstrates that the cGANN can recover the proper line shapes from the noisy experimental spectra while nearly eliminating background noise, vertical banding, and baseline shifts that result from shot-to-shot noise as well as recover the NLS decay within an error of ∼15%. The increased peak width in the reconstructed spectra does not appear to affect the initial NLS values in the analysis. However, it is possible that a model could contain a bias in the NLS, and for that reason, the training set should be constructed appropriately. In conclusion, we demonstrated the capabilities of the cGANN approach to extract dynamics from highly noisy experimental spectra of a single-peak vibrational probe. Most importantly, we demonstrated that the NLS can be extracted from noisy data that could not otherwise be analyzed.

General Considerations for Denoising Spectra Using cGANNs. In principle, the cGANN approach described here can be used to denoise a wide range of multidimensional spectra, not only 2D IR spectra but also 2D visible or extreme cross-peak spectra. Here, we provide a set of recommendations as a guide for the generation of data sets and application of the cGANN approach presented.

(1) The training set must contain the same type of noise as the experimental spectra. For example, in 2D IR spectroscopy, shot-to-shot fluctuations are often much greater compared to pixel-to-pixel noise; however, this may not be the case for other techniques. Therefore, it is important to collect "blank" shots, which contain the same noise characteristics as the experimental spectra and perform the same subtraction and averaging on the blank shots as the experimentally measured spectra.

(2) One important consideration is that the training data set must contain the same features present in the experimental data set. For instance, to reconstruct spectra containing cross-peaks, the training set must also contain cross-peaks. This is best accomplished using a response-function approach, as presented above, to generate synthetic spectra. For example, one could collect one "clean" spectrum at a single delay, use that data to fit a set of response function parameters, and subsequently use the parameter set to generate synthetic spectra.

(3) Similarly, the spectra must contain peaks of varying amplitudes, center frequencies, and widths. The training set should contain a range of peaks to avoid biasing the cGANN toward one particular feature. For example, if the peaks in the training set are too broad compared to the experimental peaks, the cGANN could be biased to produce peaks that may be too broad. Similarly, to obtain accurate NLS decays, a range of waiting times must be selected, and the correlation times should be similar to what is expected in the experiment. One would likely not know the exact correlation time prior to the measurements, but an estimate should be made to avoid biasing the cGANN. The cGANN bias can be benchmarked using synthetic spectra or experimental spectra collected at low and high signal-to-noise ratios.

(4) The training set should contain spectra with varying levels of noise. Here, we selected different levels of SNRs, 2, 5, 10, and 20, and each batch of 1000 spectra contained 250 spectra of each level. This ensures that the cGANN performs optimally with input spectra of different noise levels.

(5) Finally, when spectra contain high levels of noise, the cGANN may not be able to accurately reconstruct the spectra. It is therefore important to perform a "hallucination test" using pure noise as the input spectra and confirm that there are no specific peaks in the

https://doi.org/10.1021/acs.jpca.2c02605
J. Phys. Chem. A XXXX, XXX, XXX−XXX

output spectra. If the output contains peaks within the expected range, it may suggest that the quality of the noisy spectra may be too poor to use as cGANN input.

CONCLUSIONS AND OUTLOOK

Noise suppression approaches are essential to continue pushing the boundaries of sensitivity in 2D spectroscopy and continue to work toward increasingly challenging samples. Shot-to-shot fluctuations are the dominant source of noise in laser spectroscopy. Thus far, referencing approaches beyond simple dual-stripe detection methods have been proposed as a means of denoising spectra. Here, we demonstrate the use of machine learning as a new tool in the spectroscopists' toolbox. This approach can be combined with other methods such as edge-pixel referencing[19] or probe-reference correlation approaches[17,18] to further enhance signal-to-noise and further reduce acquisition times. The method presented here is general to any spectra, but it is important to understand which features are present in the spectra in order to generate the training set. In principle, the cGANN can be used to denoise more complex spectra that include partially overlapping peaks or cross peaks. However, the Kubo line shapes for such spectra would include a large number of parameters, and properly sampling the parameter space may be challenging. In this case, a larger training set with some "ground truth" control spectra would be recommended to ensure that the model is capable of properly capturing the line shapes present in the experimental spectra. In addition, this denoising approach can also be combined with any desired analysis including CLS, NLS, or even further machine-learning approaches to extract parameters from the reconstructed line shapes.[73]

ASSOCIATED CONTENT

Supporting Information

The Supporting Information is available free of charge at https://pubs.acs.org/doi/10.1021/acs.jpca.2c02605.

Reference to the GitHub repository containing the MATLAB training and analysis scripts and synthetic and experimental spectra; synthetic single-peak spectra generated at select waiting times with signal-to-noise ratios of 2 and 5 and no noise; cGANN-reconstructed spectra from the noisy synthetic spectra; noisy experimental 2D IR spectra collected at select waiting times and the corresponding averaged reference spectra; cGANN-reconstructed spectra from the noisy experimental spectra; comparison of the pump-slice amplitudes and probe-axis projections of the noisy, reference, and cGANN-reconstructed spectra at 1000 and 3000 fs (PDF)

AUTHOR INFORMATION

Corresponding Author

Carlos R. Baiz − *Department of Chemistry, University of Texas, Austin, Texas 78712, United States;* orcid.org/0000-0003-0699-8468; Email: cbaiz@cm.utexas.edu

Author

Ziareena A. Al-Mualem − *Department of Chemistry, University of Texas, Austin, Texas 78712, United States;* orcid.org/0000-0001-9857-5360

Complete contact information is available at: https://pubs.acs.org/10.1021/acs.jpca.2c02605

Notes

The authors declare no competing financial interest.

ACKNOWLEDGMENTS

We gratefully acknowledge financial support from the Welch Foundation (F-1891) and NSF-CAREER (CHE-1847199). Z.A.A. was supported by a UT Austin Provost Graduate Excellence Fellowship. We thank Alexander Billiot (UT Austin) for insightful discussions on the pix2pix implementation.

REFERENCES

(1) Cho, M. *Two-Dimensional Optical Spectroscopy*; Taylor & Francis Group: Boca Raton, FL, 2009.
(2) Mukamel, S. *Principles of Nonlinear Optical Spectroscopy*; Oxford University Press, 1999.
(3) Hamm, P.; Zanni, M. *Concepts and Methods of 2D Infrared Spectroscopy*; Cambridge University Press: New York, 2011.
(4) Griffith, J. A. R. Laser Heterodyne Spectroscopy. *Philos. Trans. R. Soc. L* **1982**, *307*, 563−571.
(5) Brazard, J.; Bizimana, L. A.; Turner, D. B. Accurate Convergence of Transient-Absorption Spectra Using Pulsed Lasers. *Rev. Sci. Instrum.* **2015**, *86* (5), 053106.
(6) Bradler, M.; Riedle, E. Temporal and Spectral Correlations in Bulk Continua and Improved Use in Transient Spectroscopy. *J. Opt. Soc. Am. B* **2014**, *31* (7), 1465.
(7) Kaindl, R. A.; Wurm, M.; Reimann, K.; Hamm, P.; Weiner, A. M.; Woerner, M. Generation, shaping, and Characterization of Intense Femtosecond Pulses Tunable from 3 to 20 mm. *J. Opt. Soc. Am. B* **2000**, *17* (12), 2086.
(8) Ciardi, G.; Berger, A.; Hamm, P.; Shalit, A. Signatures of Intra- And Intermolecular Vibrational Coupling in Halogenated Liquids Revealed by Two-Dimensional Raman-Terahertz Spectroscopy. *J. Phys. Chem. Lett.* **2019**, *10* (15), 4463−4468.
(9) Shalit, A.; Mousavi, S. J.; Hamm, P. 2D Raman-THz Spectroscopy of Binary CHBr3-MeOH Solvent Mixture. *J. Phys. Chem. B* **2021**, *125* (2), 581−586.
(10) Flanagan, J. C.; Baiz, C. R. Site-Specific Peptide Probes Detect Buried Water in a Lipid Membrane. *Biophys. J.* **2019**, *116* (9), 1692−1700.
(11) Schmidt-Engler, J. M.; Blankenburg, L.; Zangl, R.; Hoffmann, J.; Morgner, N.; Bredenbeck, J. Local Dynamics of the Photo-Switchable Protein PYP in Ground and Signalling State Probed by 2D-IR Spectroscopy of -SCN Labels. *Phys. Chem. Chem. Phys.* **2020**, *22* (40), 22963−22972.
(12) Wilson, K. S.; Mapile, A. N.; Wong, C. Y. Broadband Single-Shot Transient Absorption Spectroscopy. *Opt. Express* **2020**, *28* (8), 11339−11355.
(13) Fuller, F. D.; Ogilvie, J. P. Experimental Implementations of Two-Dimensional Fourier Transform Electronic Spectroscopy. *Annu. Rev. Phys. Chem.* **2015**, *66*, 667−690.
(14) Kearns, N. M.; Mehlenbacher, R. D.; Jones, A. C.; Zanni, M. T. Broadband 2D Electronic Spectrometer Using White Light and Pulse Shaping: Noise and Signal Evaluation at 1 and 100 kHz. *Opt. Express* **2017**, *25* (7), 7869.
(15) Harel, E.; Fidler, A. F.; Engel, G. S. Single-Shot Gradient-Assisted Photon Echo Electronic Spectroscopy. *J. Phys. Chem. A* **2011**, *115* (16), 3787−3796.
(16) Dunbar, J. A.; Osborne, D. G.; Anna, J. M.; Kubarych, K. J. Accelerated 2D-IR Using Compressed Sensing. *J. Phys. Chem. Lett.* **2013**, *4* (15), 2489−2492.
(17) Feng, Y.; Vinogradov, I.; Ge, N.-H. General Noise Suppression Scheme with Reference Detection in Heterodyne Nonlinear Spectroscopy. *Opt. Express* **2017**, *25* (21), 26262.
(18) Feng, Y.; Vinogradov, I.; Ge, N.-H. Optimized Noise Reduction Scheme for Heterodyne Spectroscopy Using Array Detectors. *Opt. Express* **2019**, *27* (15), 20323.

(19) Robben, K. C.; Cheatum, C. M. Edge-Pixel Referencing Suppresses Correlated Baseline Noise in Heterodyned Spectroscopies. *J. Chem. Phys.* **2020**, *152* (9), 094201.
(20) Farrell, K.; Ostrander, J.; Jones, A.; Yakami, B.; Dicke, S.; Middleton, C.; Hamm, P.; Zanni, M. Shot-to-Shot 2D IR Spectroscopy at 100 kHz Using a Yb Laser and Custom Designed Electronics. *Opt. Express* **2020**, *28* (22), 33584−33602.
(21) Kübel, J.; Westenhoff, S.; Maj, M. Giving Voice to the Weak: Application of Active Noise Reduction in Transient Infrared Spectroscopy. *Chem. Phys. Lett.* **2021**, *783*, 139059.
(22) Kruiger, J. F.; Van Der Vegte, C. P.; Jansen, T. L. C. Suppressing Sampling Noise in Linear and Two-Dimensional Spectral Simulations. *J. Chem. Phys.* **2015**, *142* (5), 054201.
(23) Rasskazov, G.; Lozovoy, V. V.; Dantus, M. Spectral Amplitude and Phase Noise Characterization of Titanium-Sapphire Lasers. *Opt. Express* **2015**, *23* (18), 23597.
(24) Bristow, A. D.; Karaiskaj, D.; Dai, X.; Zhang, T.; Carlsson, C.; Hagen, K. R.; Jimenez, R.; Cundiff, S. T. A Versatile Ultrastable Platform for Optical Multidimensional Fourier-Transform Spectroscopy. *Rev. Sci. Instrum.* **2009**, *80* (7), 073108.
(25) Hill, R. J.; Courtney, T. L.; Park, S. D.; Jonas, D. M. Lightweight Hollow Rooftop Mirrors for Stabilized Interferometry. *Opt. Eng.* **2013**, *52* (10), 105103.
(26) Zhu, W.; Wang, R.; Zhang, C.; Wang, G.; Liu, Y.; Zhao, W.; Dai, X.; Wang, X.; Cerullo, G.; Cundiff, S.; et al. Broadband Two-Dimensional Electronic Spectroscopy in an Actively Phase Stabilized Pump-Probe Configuration. *Opt. Express* **2017**, *25* (18), 21115.
(27) Donaldson, P. M.; Greetham, G. M.; Shaw, D. J.; Parker, A. W.; Towrie, M. A 100 kHz Pulse Shaping 2D-IR Spectrometer Based on Dual Yb:KGW Amplifiers. *J. Phys. Chem. A* **2018**, *122* (3), 780−787.
(28) Farrell, K.; Ostrander, J.; Jones, A.; Yakami, B.; Dicke, S.; Middleton, C.; Hamm, P.; Zanni, M. Shot-to-Shot 2D IR Spectroscopy at 100 kHz Using a Yb Laser and Custom-Designed Electronics. *Opt. Express* **2020**, *28* (22), 33584−33602.
(29) Kanal, F.; Keiber, S.; Eck, R.; Brixner, T. 100-kHz Shot-to-Shot Broadband Data Acquisition for High-Repetition-Rate Pump−Probe Spectroscopy. *Opt. Express* **2014**, *22* (14), 16965.
(30) Auböck, G.; Consani, C.; Monni, R.; Cannizzo, A.; Van Mourik, F.; Chergui, M. Femtosecond Pump/Supercontinuum-Probe Setup with 20 kHz Repetition Rate Repetition Rate. *Rev. Sci. Instrum.* **2012**, *83*, 093105.
(31) Jeon, J.; Kim, J.; Yoon, T. H.; Cho, M. Dual Frequency Comb Photon Echo Spectroscopy. *J. Opt. Soc. Am. B* **2019**, *36* (2), 223.
(32) Lomsadze, B.; Cundiff, S. T. Frequency Combs Enable Rapid and High-Resolution Multidimensional Coherent Spectroscopy. *Science* **2017**, *357* (6358), 1389−1391.
(33) Dobryakov, A. L.; Kovalenko, S. A.; Weigel, A.; Prez-Lustres, J. L.; Lange, J.; Müller, A.; Ernsting, N. P. Femtosecond Pump/Supercontinuum-Probe Spectroscopy: Optimized Setup and Signal Analysis for Single-Shot Spectral Referencing. *Rev. Sci. Instrum.* **2010**, *81* (11), 113106.
(34) Krebs, N.; Pugliesi, I.; Hauer, J.; Riedle, E. Two-Dimensional Fourier Transform Spectroscopy in the Ultraviolet with Sub-20 fs Pump Pulses and 250−720 nm Supercontinuum Probe. *New J. Phys.* **2013**, *15*, 085016.
(35) Ruckebusch, C.; Sliwa, M.; Pernot, P.; de Juan, A.; Tauler, R. Comprehensive Data Analysis of Femtosecond Transient Absorption Spectra: A Review. *J. Photochem. Photobiol. C Photochem. Rev.* **2012**, *13* (1), 1−27.
(36) Jordan, M. I.; Mitchell, T. M. Machine Learning: Trends, Perspectives, and Prospects. *Science* **2015**, *349* (6245), 255−260.
(37) Kumar, A.; Bi, L.; Kim, J.; Feng, D. D. Machine Learning in Medical Imaging. In *Biomedical Information Technology*; Elsevier Inc., 2020; pp 167−196; DOI: 10.1016/b978-0-12-816034-3.00005-5.
(38) Kermany, D. S.; Goldbaum, M.; Cai, W.; Valentim, C. C. S.; Liang, H.; Baxter, S. L.; McKeown, A.; Yang, G.; Wu, X.; Yan, F.; et al. Identifying Medical Diagnoses and Treatable Diseases by Image-Based Deep Learning. *Cell* **2018**, *172* (5), 1122−1131.E9.
(39) Helgadottir, S.; Argun, A.; Volpe, G. Digital Video Microscopy Enhanced by Deep Learning. *Optica* **2019**, *6* (4), 506.
(40) Abiodun, O. I.; Jantan, A.; Omolara, A. E.; Dada, K. V.; Mohamed, N. A. E.; Arshad, H. State-of-the-Art in Artificial Neural Network Applications: A Survey. *Heliyon* **2018**, *4* (11), No. e00938.
(41) Singh, K.; Seth, A.; Sandhu, H. S.; Samdani, K. A Comprehensive Review of Convolutional Neural Network Based Image Enhancement Techniques. *2019 IEEE International Conference on System, Computation, Automation and Networking (ICSCAN)* **2019**, 1−6.
(42) Parekh, J.; Turakhia, P.; Bhinderwala, H.; Dhage, S. N. A Survey of Image Enhancement and Object Detection Methods. In *Advances in Computer, Communication and Computational Sciences*; Advances in Intelligent Systems and Computing; Springer, 2021; Vol. *1158*.
(43) Lin, Q.; Fouchez, D.; Pasquet, J. Galaxy Image Translation with Semi-Supervised Noise-Reconstructed Generative Adversarial Networks. *2020 25th International Conference on Pattern Recognition (ICPR)* **2021**, 5634−5641.
(44) Goodfellow, I.; Pouget-Abadie, J.; Mirza, M.; Xu, B.; Warde-Farley, D.; Ozair, S.; Courville, A.; Bengio, Y. Generative Adversarial Nets. In *NeurIPS Proceedings*; 2014; pp 2672−2680; https://proceedings.neurips.cc/paper/2014/file/5ca3e9b122f61f8f06494c97b1afccf3-Paper.pdf.
(45) Schonfeld, E.; Schiele, B.; Khoreva, A. A U-Net Based Discriminator for Generative Adversarial Networks. *2020 IEEE/CVF Conference on Computer Vision and Pattern Recognition (CVPR)* **2020**, 8204−8213.
(46) Creswell, A.; White, T.; Dumoulin, V.; Arulkumaran, K.; Sengupta, B.; Bharath, A. A. Generative Adversarial Network: An Overview. *IEEE Signal Process. Mag* **2018**, *35*, 53−65.
(47) Mirza, M.; Osindero, S. Conditional Generative Adversarial Nets. *arXiv*, **2014**, arXiv:1411.1784.
(48) Isola, P.; Zhu, J. Y.; Zhou, T.; Efros, A. A. Image-to-Image Translation with Conditional Adversarial Networks. *2017 IEEE Conference on Computer Vision and Pattern Recognition (CVPR)* **2017**, 5967−5976.
(49) Edington, S. C.; Gonzalez, A.; Middendorf, T. R.; Halling, D. B.; Aldrich, R. W.; Baiz, C. R. Coordination to Lanthanide Ions Distorts Binding Site Conformation in Calmodulin. *Proc. Natl. Acad. Sci.* **2018**, *115* (14), E3126−E3134.
(50) Shim, S. H.; Zanni, M. T. How to Turn Your Pump-Probe Instrument into a Multidimensional Spectrometer: 2D IR and Vis Spectroscopies via Pulse Shaping. *Phys. Chem. Chem. Phys.* **2009**, *11* (5), 748−761.
(51) Ghosh, A.; Serrano, A. L.; Oudenhoven, T. A.; Ostrander, J. S.; Eklund, E. C.; Blair, A. F.; Zanni, M. T. Experimental Implementations of 2D IR Spectroscopy through a Horizontal Pulse Shaper Design and a Focal Plane Array Detector. *Opt. Lett.* **2016**, *41* (3), 524.
(52) Valentine, M. L.; Waterland, M. K.; Fathizadeh, A.; Elber, R.; Baiz, C. R. Interfacial Dynamics in Lipid Membranes: The Effects of Headgroup Structures. *J. Phys. Chem. B* **2021**, *125* (5), 1343−1350.
(53) Baiz, C. R.; Kubarych, K. J.; Geva, E.; Sibert, E. L. Local-Mode Approach to Modeling Multidimensional Infrared Spectra of Metal Carbonyls. *J. Phys. Chem. A* **2011**, *115* (21), 5354−5363.
(54) Sun, X.; Geva, E. Non-Condon Nonequilibrium Fermi's Golden Rule Rates from the Linearized Semiclassical Method. *J. Chem. Phys.* **2016**, *145* (6), 064109.
(55) Schmidt, J. R.; Corcelli, S. A.; Skinner, J. L. Pronounced Non-Condon Effects in the Ultrafast Infrared Spectroscopy of Water. *J. Chem. Phys.* **2005**, *123* (4), 044513.
(56) Radford, A.; Metz, L.; Chintala, S. Unsupervised Representation Learning with Deep Convolutional Generative Adversarial Networks. *arXiv*, **2016**, arXiv:1511.06434v2.
(57) Jonas, D. M. Two-Dimensional Femtosecond Spectroscopy. *Annu. Rev. Phys. Chem.* **2003**, *54*, 425−463.
(58) Valentine, M. L.; Al-Mualem, Z. A.; Baiz, C. R. Pump Slice Amplitudes: A Simple and Robust Method for Connecting Two-

https://doi.org/10.1021/acs.jpca.2c02605
J. Phys. Chem. A XXXX, XXX, XXX−XXX

Dimensional Infrared and Fourier Transform Infrared Spectra. *J. Phys. Chem. A* **2021**, *125* (29), 6498−6504.
(59) Fayer, M. D. Dynamics of Liquids, Molecules, and Proteins Measured with Ultrafast 2D IR Vibrational Echo Chemical Exchange Spectroscopy. *Annu. Rev. Phys. Chem.* **2009**, *60*, 21−38.
(60) Reppert, M.; Tokmakoff, A. Computational Amide i 2D IR Spectroscopy as a Probe of Protein Structure and Dynamics. *Annu. Rev. Phys. Chem.* **2016**, *67*, 359−386.
(61) Fayer, M. D. *Ultrafast Infrared Vibrational Spectroscopy*, 1st ed.; CRC Press, 2013.
(62) Ghosh, A.; Ostrander, J. S.; Zanni, M. T. Watching Proteins Wiggle: Mapping Structures with Two-Dimensional Infrared Spectroscopy. *Chem. Rev.* **2017**, *117* (16), 10726−10759.
(63) Flanagan, J. C.; Valentine, M. L.; Baiz, C. R. Ultrafast Dynamics at Lipid−Water Interfaces. *Acc. Chem. Res.* **2020**, *53* (9), 1860−1868.
(64) Kwac, K.; Cho, M. Molecular Dynamics Simulation Study of N-Methylacetamide in Water. II. Two-Dimensional Infrared Pump-Probe Spectra. *J. Chem. Phys.* **2003**, *119* (4), 2256−2263.
(65) Kwak, K.; Park, S.; Finkelstein, I. J.; Fayer, M. D. Frequency-Frequency Correlation Functions and Apodization in Two-Dimensional Infrared Vibrational Echo Spectroscopy: A New Approach. *J. Chem. Phys.* **2007**, *127* (12), 124503.
(66) Simpson, N.; Hunt, N. T. Ultrafast 2D-IR Spectroscopy of Haemoproteins. *Int. Rev. Phys. Chem.* **2015**, *34* (3), 361−383.
(67) Guo, Q.; Pagano, P.; Li, Y. L.; Kohen, A.; Cheatum, C. M. Line Shape Analysis of Two-Dimensional Infrared Spectra. *J. Chem. Phys.* **2015**, *142* (21), 212427.
(68) Kwak, K.; Rosenfeld, D. E.; Fayer, M. D. Taking Apart the Two-Dimensional Infrared Vibrational Echo Spectra: More Information and Elimination of Distortions. *J. Chem. Phys.* **2008**, *128* (20), 204505.
(69) Fenn, E. E.; Fayer, M. D. Extracting 2D IR Frequency-Frequency Correlation Functions from Two Component Systems. *J. Chem. Phys.* **2011**, *135* (7), 074502.
(70) Kramer, P. L.; Nishida, J.; Fayer, M. D. Separation of Experimental 2D IR Frequency-Frequency Correlation Functions into Structural and Reorientation-Induced Contributions. *J. Chem. Phys.* **2015**, *143* (12), 124505.
(71) Duan, R.; Mastron, J. N.; Song, Y.; Kubarych, K. J. Direct Comparison of Amplitude and Geometric Measures of Spectral Inhomogeneity Using Phase-Cycled 2D-IR Spectroscopy. *J. Chem. Phys.* **2021**, *154* (17), 174202.
(72) Baryiames, C. P.; Teel, M.; Baiz, C. R. Interfacial H-Bond Dynamics in Reverse Micelles: The Role of Surfactant Heterogeneity. *Langmuir* **2019**, *35* (35), 11463−11470.
(73) Hoffman, D. J.; Fayer, M. D. CLS Next Gen: Accurate Frequency-Frequency Correlation Functions from Center Line Slope Analysis of 2D Correlation Spectra Using Artificial Neural Networks. *J. Phys. Chem. A* **2020**, *124* (28), 5979−5992.

https://doi.org/10.1021/acs.jpca.2c02605
J. Phys. Chem. A XXXX, XXX, XXX−XXX